ACS APPLIED MATERIALS & INTERFACES

www.acsami.org Research Article

Tuning the Properties of Halide Nanocomposite Solid Electrolytes with Diverse Oxides for All-Solid-State Batteries

Hiram Kwak, Jong Seok Kim, Daseul Han, Jae-Seung Kim, Juhyoun Park, Changhoon Kim, Dong-Hwa Seo, Kyung-Wan Nam, and Yoon Seok Jung*

Cite This: *ACS Appl. Mater. Interfaces* 2024, 16, 49328−49336 Read Online

ACCESS | Metrics & More | Article Recommendations | Supporting Information

ABSTRACT: Herein, we report halide nanocomposite solid electrolytes (HNSEs) that integrate diverse oxides with alterations that allow tuning of their ionic conductivity, (electro)chemical stability, and specific density. A two-step mechanochemical process enabled the synthesis of multimetal (or nonmetal) HNSEs, $MO_2-2Li_2ZrCl_6$, as verified by pair distribution function and X-ray diffraction analyses. The multimetal (or nonmetal) HNSE strategy increases the ionic conductivity of Li_2ZrCl_6 from 0.40 to 0.82 mS cm^{-1}. Additionally, cyclic voltammetry test findings corroborated the enhanced passivating properties of the HNSEs. Notably, incorporating SiO_2 into HNSEs leads to a substantial reduction in the specific density of HNSEs, demonstrating their strong potential for achieving a high energy density and lowering costs. Fluorinated $SiO_2-2Li_2ZrCl_5F$ HNSEs exhibited enhanced interfacial compatibility with Li_6PS_5Cl and $LiCoO_2$ electrodes. Cells employing $SiO_2-2Li_2ZrCl_5F$ with $LiCoO_2$ exhibit superior electrochemical performance delivering the initial discharge capacity of 162 mA h g^{-1} with 93.7% capacity retention at the 100th cycle at 60 °C.

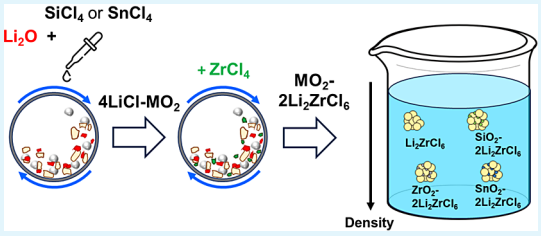

KEYWORDS: *all-solid-state batteries, halide solid electrolytes, ionic conductivities, interfacial conduction, Li-ion batteries*

Downloaded via YONSEI UNIV on September 19, 2024 at 08:48:01 (UTC).
See https://pubs.acs.org/sharingguidelines for options on how to legitimately share published articles.

1. INTRODUCTION

The constraints on energy density and safety inherent in conventional lithium-ion batteries, primarily owing to their reliance on liquid electrolytes, have stimulated the development of all-solid-state batteries (ASSBs).[1−9] These batteries use nonflammable inorganic solid electrolytes (SEs), presenting a potential pathway to enable Li metal or Si anodes.[1−8,10−22] Among the SE candidates, sulfide SEs, including variants of Li argyrodite (e.g., $Li_{6-y}PS_{5-y}X_{1+y}$ (where X = Cl, Br; y = 0.0−0.5)), are particularly promising.[23,24] These SEs provide high ionic conductivities ranging from 1 to 10 mS cm^{-1} at 25 °C, comparable to those of liquid electrolytes, while also benefiting from mechanical sinterability.[7,23−29] However, they are limited by poor electrochemical oxidative thresholds (∼2.6 V vs Li/Li^+),[25−28,30−32] which results in compromised electrochemical performance when paired with uncoated 4 V class layered cathode materials ($LiMO_2$, M = Ni, Co, Mn, or Al). Moreover, oxide SEs, such as $Li_7La_3Zr_2O_{12}$, while offering commendable (electro)chemical oxidative stability, have their own challenges.[33] Their inherent brittleness complicates the fabrication of ASSBs, barring the use of hybrid systems that incorporate liquid or soft ion conductors.[34,35]

However, the development of mechanochemically prepared trigonal Li_3YCl_6,[36] with reasonable Li^+ conductivity (0.51 mS cm^{-1} at 25 °C), noteworthy mechanical deformability, and compatibility with uncoated $LiCoO_2$ in ASSB cells, reignited interest in halide SEs,[16,17,36−38] leading to the identification of novel compositions, such as Li_3MCl_6-type halide SEs (M = In, Sc, Yb and Li^+ conductivities ranging of 0.1−3 mS cm^{-1} at 25 °C).[39−42] Notably, preparing these Li_3MCl_6-type materials involves the incorporation of rare earth metals or other expensive components, which hinders their practical applicability. However, Li_2ZrCl_6 and its derivatives (e.g., $Li_{2+x}Zr_{1-x}M_xCl_6$ (M = Fe, Cr, V), ∼1.0 mS cm^{-1} at 30 °C) stand as exceptions.[43] Furthermore, the X-ray diffraction (XRD)-amorphous halide SEs incorporating Nb or Ta with exceptional ionic conductivities reaching up to 10 mS cm^{-1} marked a significant development.[44−46] These SEs are characterized by their polyhedral units based on pentavalent cations, which prefer corner-sharing arrangements rather than edge- or face-sharing, contributing to a flattened Li^+ migration energy landscape with low migration energy.[45−47] Moreover, halide SEs comprising MCl_3 (M = La−Gd) and Li halide compounds have been suggested.[48,49]

Consistent with the strategies used for other inorganic superionic conductors,[7,24,50] compositional tuning through alio- or iso-valent substitution has been a common practice for enhancing the ionic conductivity of halide SEs.[43,51−53] This

Received: May 30, 2024
Revised: July 24, 2024
Accepted: August 20, 2024
Published: September 4, 2024

© 2024 American Chemical Society

https://doi.org/10.1021/acsami.4c08915
ACS Appl. Mater. Interfaces 2024, 16, 49328−49336

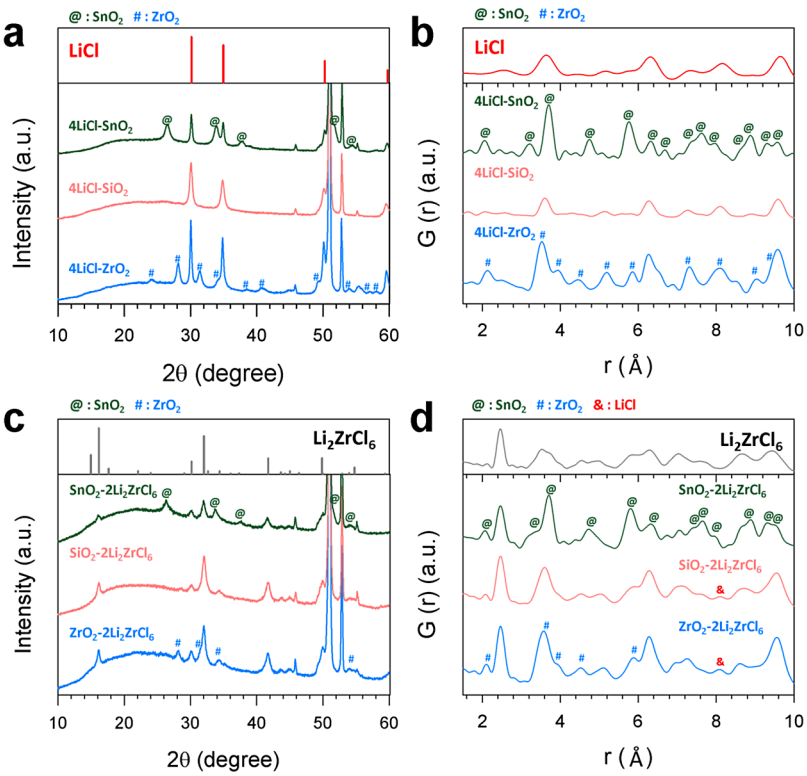

Figure 1. Structural characterization of HNSEs. (a) XRD patterns and (b) PDF $G(r)$ for 4LiCl−ZrO_2, 4LiCl−SiO_2, and 4LiCl−SnO_2. The Bragg indices and PDF $G(r)$ for LiCl are shown at the top in (a, b), respectively. (c) XRD patterns and (d) PDF $G(r)$ for ZrO_2−$2Li_2ZrCl_6$, SiO_2−$2Li_2ZrCl_6$, and SnO_2−$2Li_2ZrCl_6$. The Bragg indices and PDF $G(r)$ for Li_2ZrCl_6 are shown at the top in parts (c) and (d), respectively.

approach involves adjusting the charge-carrier concentration and/or lattice frameworks.[7,24,43,50,54] Notable examples of this strategy include the monoclinic system ($Li_{3-x}M_{1-x}Zr_xCl_6$, M = In, Sc, max. 2.1 mS cm^{-1} at 30 °C),[51] trigonal or orthorhombic system ($Li_{3-x}M_{1-x}Zr_xCl_6$, M = Y, Er, max. 1.4 mS cm^{-1} at 25 °C,[52] $Li_{2+x}Zr_{1-x}M_xCl_6$, M = Fe, Cr, V, max. 1.0 mS cm^{-1} at 30 °C,[43] and $Li_{3-x}Yb_{1-x}M_xCl_6$, M = Zr, Hf, max. 1.5 mS cm^{-1} at 30 °C[55]). Additionally, structural disorder such as metal site disorder (involving Y, Er, and Zr) and stacking faults, which depend on the preparation technique, have been recognized as crucial factors affecting the ionic conductivity of halide solid electrolytes.[56−58]

Recently, we introduced halide nanocomposite SEs (HNSEs) ZrO_2(−ACl)−A_2ZrCl_6 (A = Li or Na) which show significantly higher ionic conductivities than their traditional counterparts A_2ZrCl_6, with increases from 0.40 to 1.3 mS cm^{-1} for Li^+ and from 0.011 to 0.11 mS cm^{-1} for Na^+.[59,60] These HNSEs also show enhanced compatibility with sulfides.[59,60] The enhanced ionic conductivities stem from the nanostructured networks comprising ZrO_2 and A_2ZrCl_6 during mechanochemical synthesis using Li_2O, resulting in enhanced interfacial superionic conduction, further attributed to the widened Li^+ transport channels and increased Li^+ concentration in the oxygen-substituted $Li_{2+x}ZrCl_{6-x}O_x$ interphases.[59,60]

Although halide SEs have the aforementioned promising features, their potential to completely replace sulfide SEs is hindered by their poor electrochemical reduction stability and comparatively high specific density.[15,17] To address their poor electrochemical reduction stability, ASSB cells that employ halide SEs as catholytes and sulfide SEs as separating SE layers, are viable for practical applications.[15,17,36,39,59,61] However, the incompatibility between halide and sulfide SEs, particularly at elevated temperatures and voltages, has emerged as a critical challenge.[59,61] Koç et al. demonstrated that parasitic chemical reactions between electrode employing Li_3InCl_6 as catholyte and Li_6PS_5Cl as separators lead to interfacial deterioration within the dual SE system.[61] This degradation causes poor cycling performance, prompting reconsideration of the design of dual SE cell configurations.

As mentioned above, the comparatively high specific density of halide SEs remains a significant concern. For instance, we demonstrated that single-crystalline $LiNi_{0.88}Co_{0.11}Al_{0.01}O_2$ with Li_3YCl_6 experienced internal cracking,[15] owing to the poor spatial distribution attributed to the high specific density of Li_3YCl_6 (2.43 vs 1.96 g cm^{-3} for LPSX) and the small particle size of single-crystalline $LiNi_{0.88}Co_{0.11}Al_{0.01}O_2$; this inhomogeneous distribution leads to unsatisfactory cycling retention. However, the challenge posed by the high density of halide SEs becomes even more conspicuous in Li_2ZrCl_6-based HNSE that incorporate high-density metal oxides such as ZrO_2 (theoretical specific density of Li_2ZrCl_6: 2.57 g cm^{-3} and ZrO_2−$2Li_2ZrCl_6$: 2.76 g cm^{-3}).

In this study, we expand the compositional space of HNSEs by exploring combinations of various metal or nonmetal oxides (MO_2−$2Li_2ZrCl_6$, M = Si, Sn, and Zr) through a two-step mechanochemical method (4LiCl−MO_2 and subsequently MO_2−$2Li_2ZrCl_6$). Comprehensive analyses using XRD and pair distribution function (PDF) measurements confirmed the presence of nanocomposite structures. The results indicated that ionic conductivity enhancement via interfacial conduction is not limited to combinations with ZrO_2 and is possible with other metal or nonmetal oxides paired with Li_2ZrCl_6. Specifically, the SiO_2−$2Li_2ZrCl_6$ HNSE is notable owing to

https://doi.org/10.1021/acsami.4c08915
ACS Appl. Mater. Interfaces 2024, 16, 49328−49336

its low density, attributed to the lightness of SiO_2 (2.65 g cm^{-3} vs 6.95 g cm^{-3} for SnO_2 or 5.68 g cm^{-3} for ZrO_2). Furthermore, the excellent compatibility of SiO_2−$2Li_2ZrCl_6$ and SiO_2−$2Li_2ZrCl_5F$ with uncoated $LiCoO_2$ and Li_6PS_5Cl markedly enhanced the electrochemical performance of ASSBs at 60 °C, offering a notable improvement over systems that utilize Li_2ZrCl_6.

2. RESULTS AND DISCUSSION

HNSEs with diverse oxides were prepared via a two-step mechanochemical reaction, as illustrated in Figure S1. In the first step, Li_2O, which serves as the oxygen source, reacts with MCl_4 (M = Zr, Si, or Sn) to form nanomixtures of MO_2 and LiCl. Using density functional theory (DFT) calculations, the formation energy of LiCl and MO_2 from Li_2O and MCl_4 was evaluated, revealing a significant driving force for Zr, Si, and Sn. Specifically, among the various competing reactions considered, the following reaction was found to be the most thermodynamically favorable (Table S1 and Figure S2): $2/3Li_2O + 1/3MCl_4 \rightarrow 4/3LiCl + 1/3MO_2$. Figure 1a shows the XRD patterns of intermediate products 4LiCl−MO_2. Both 4LiCl−SnO_2 and 4LiCl−ZrO_2 display patterns corresponding to the Bragg indices of LiCl and the respective metal oxides. However, 4LiCl−SiO_2 reveals only LiCl patterns, suggesting the presence of amorphous SiO_2. Figure S3 presents scanning electron microscopy (SEM) and corresponding energy dispersive X-ray spectroscopy (EDXS) mapping images of LiCl and MO_2 particles, showing a uniform distribution of Si, O, and Cl on the 4LiCl−SiO_2 particles. The transmission electron microscopy (TEM) images with their corresponding EDXS maps for 4LiCl−SiO_2 (Figure S4) reveal that particles represented by green, indicating Si, are embedded within regions depicted in red, signifying Cl. At higher magnification in the TEM images (Figure S4e,f), LiCl nanograins with their corresponding fast Fourier transform (FFT) patterns are displayed, yet the crystalline structure of SiO_2 is absent. Given that SiO_2 is produced by oxidizing $SiCl_4$,[62−64] 4LiCl−SiO_2 could be inferred to consist of crystalline LiCl and amorphous SiO_2. Figure 1b shows the PDF $G(r)$ profiles of 4LiCl−SiO_2, 4LiCl−ZrO_2, and 4LiCl−SnO_2. Consistent with the XRD results, all of the PDF signals demonstrate the presence of LiCl, along with the identifiable crystalline structures of ZrO_2 and SnO_2. However, the SiO_2 structures remain undiscernible. The amorphous nature of SiO_2 nanoparticles is noted by the absence of a long-range ordered structure,[65−67] further highlighted by a significant amount of local disorder, particularly evident in the variations in the Si−O−Si angles and the mean lengths of the Si−O bonds. These variations contributed to the broadening of the peaks in the PDF spectra, complicating the precise identification of specific peaks in these structures. In the second step, $ZrCl_4$ is introduced into the previously formed 4LiCl−MO_2 powder, and the mixture is mechanochemically milled. This process yields the final products of ZrO_2−$2Li_2ZrCl_6$, SiO_2−$2Li_2ZrCl_6$, and SnO_2−$2Li_2ZrCl_6$ HNSEs. Figure 1c,d confirm the presence of Li_2ZrCl_6 in all of the XRD and PDF analyses, along with crystalline ZrO_2 and SnO_2 in the respective HNSEs, while the amorphous nature of SiO_2 persists in alignment with the initial stage.

The ionic conductivity results of the HNSEs, determined by the AC impedance method using ion-blocking symmetric cells (Ti|Halide SE or HNSE|Ti), are shown in Figure 2, with the Nyquist plots in Figure 2a fitted by using the equivalent circuit model presented in Figure S5. Figure 2b displays the corresponding Arrhenius plots of the Li^+ conductivity. Compared with Li_2ZrCl_6, all HNSEs exhibited enhanced Li^+ conductivities: ZrO_2−$2Li_2ZrCl_6$: 0.71 mS cm^{-1}, SiO_2−$2Li_2ZrCl_6$: 0.69 mS cm^{-1}, and SnO_2−$2Li_2ZrCl_6$: 0.82 mS cm^{-1} vs Li_2ZrCl_6: 0.47 mS cm^{-1}. Furthermore, a modest reduction in the activation energy was observed for ZrO_2−$2Li_2ZrCl_6$: 0.36 eV, SiO_2−$2Li_2ZrCl_6$: 0.36 eV, and SnO_2−$2Li_2ZrCl_6$: 0.35 eV vs Li_2ZrCl_6: 0.39 eV. These results are noteworthy, considering the incorporation of ionically insulating oxides into the HNSEs. In contrast to traditional AX (where A = Li, Cu, Ag and X = Cl, Br, I) with metal oxide systems, which often achieve high ionic conductivities due to the space charge layer (SCL) effect,[68−70] the enhanced ionic conduction in HNSEs is primarily due to structural changes at the interface.[59,60] In our previous study,[59] using DFT and ab initio molecular dynamics simulations, we revealed that a small anion exchange at the ZrO_2/Li_2ZrCl_6 interface in the ZrO_2−$2Li_2ZrCl_6$ forms partially oxidized $Li_{2.5}ZrCl_{5.5}O_{0.5}$ with enhanced Li^+ diffusivity compared to Li_2ZrCl_6. Experimental evidence supported the presence of this $Li_{2.5}ZrCl_{5.5}O_{0.5}$ interphase. In light of these results, the formation of partially oxidized Li_2ZrCl_6 species at the interface between ZrO_2, SiO_2,

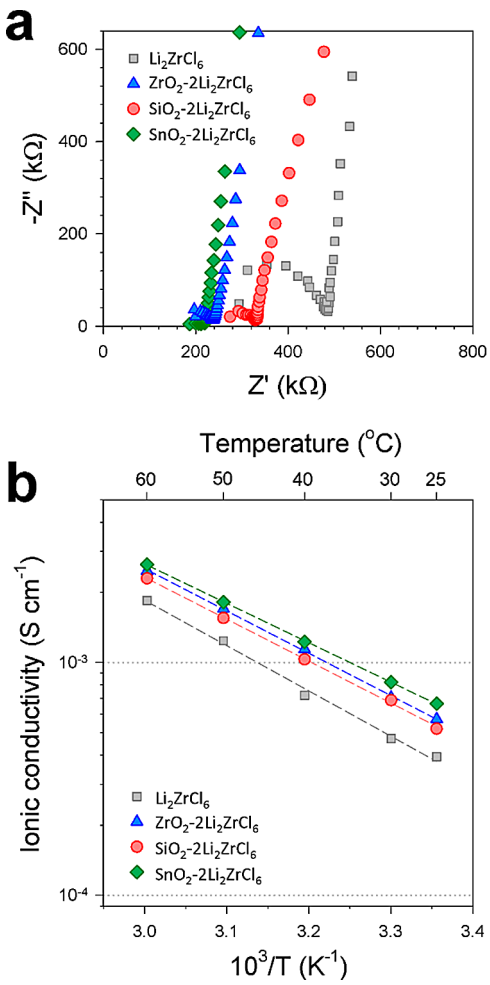

Figure 2. Ionic conductivities of Li_2ZrCl_6 and HNSEs. (a) Nyquist plots of Ti|Halide SE or HNSE|Ti symmetric cells for Li_2ZrCl_6 and HNSEs (MO_2−$2Li_2ZrCl_6$ (M = Zr, Si, and Sn)). (b) Arrhenius plots of ionic conductivities for Li_2ZrCl_6 and the HNSEs.

https://doi.org/10.1021/acsami.4c08915
ACS Appl. Mater. Interfaces 2024, 16, 49328−49336

or SnO_2/Li_2ZrCl_6 would contribute to the observed increase in ionic conductivity.

The specific densities of the various HNSEs with different oxides were determined by using the Archimedes method, with the results shown in Figure 3. The specific density for Li_2ZrCl_6

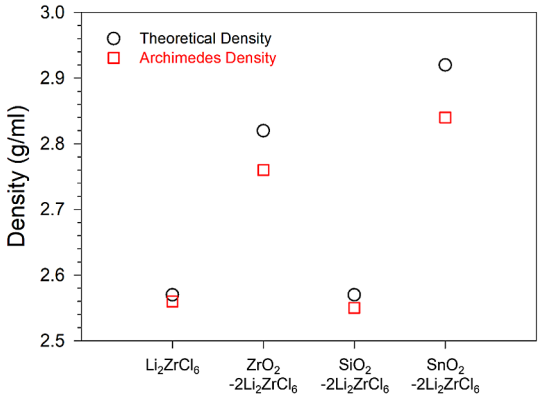

Figure 3. Theoretical and experimental densities of Li_2ZrCl_6 and HNSEs ($MO_2-2Li_2ZrCl_6$ (M = Zr, Si, and Sn)).

was 2.56 g cm^{-3}, which is consistent with the theoretical value of 2.57 g cm^{-3}, as measured experimentally. However, integrating Li_2ZrCl_6 with heavy metal oxides of ZrO_2 (5.86 g cm^{-3}) or SnO_2 (6.95 g cm^{-3}) significantly raised the specific density to 2.76 and 2.84 g cm^{-3}, respectively. Conversely, incorporating a lighter oxide SiO_2 (2.65 g cm^{-3}) led to a marginal difference in the specific density (2.55 g cm^{-3}) while maintaining the enhanced Li^+ conductivity. This balance translates into an increase in power density, not offset by a decreased energy density for ASSB cells.[2,5,15,50,71] Notably, for all HNSEs, the experimentally measured specific densities were strongly consistent with the theoretical values calculated based on a mixture of Li_2ZrCl_6 and MO_2, thus confirming the successful formation of nanocomposite mixtures.

To assess the (electro)chemical stability of Li_2ZrCl_6 and various HNSEs, cyclic voltammetry (CV) tests were conducted at 0.1 mV s^{-1} and 30 °C, using (SE-C)|Li_6PS_5Cl|(Li−In) cells ranging from 3.0 to 5.0 V (vs Li/Li^+), with the results displayed in Figure 4 and Table S2. During the initial cycle, Li_2ZrCl_6 showed a substantial integrated anodic current of 2.78 mA V g^{-1} (~5.0 V vs Li/Li^+), which remained significantly high in the subsequent cycle at 2.04 mA V g^{-1}. Moreover, in the first cycle, Li_2ZrCl_6 exhibited a cathodic peak around 3.5 V (vs Li/Li^+), which intensified in the second cycle. The anodic and cathodic currents registered in the CV tests are attributed to the decomposition of halide SEs at high voltages and the reactions between halide SEs and Li_6PS_5Cl, employed as the separating SE layer, respectively.[59,61,72,73] Prior research indicated that anion exchange, along with the decomposition of each SE, occurs at the interface between halide and sulfide SE.[59,61,72,73] The $SiO_2-2Li_2ZrCl_6$ HNSE initially showed a larger integrated current of 4.40 mA V g^{-1} during the first cycle, surpassing that of Li_2ZrCl_6 (2.78 mA V g^{-1}).

However, this value decreased significantly in the second cycle, dropping to 0.55 mA V g^{-1} for $SiO_2-2Li_2ZrCl_6$ compared to 2.00 mA V g^{-1} for Li_2ZrCl_6. Additionally, $SiO_2-2Li_2ZrCl_6$ registered negligible cathodic currents, a trend consistent across all of the HNSE samples. According to Koç et al.,[61] the chemical incompatibility between halide and sulfide SEs can be addressed by applying a thin protective layer of

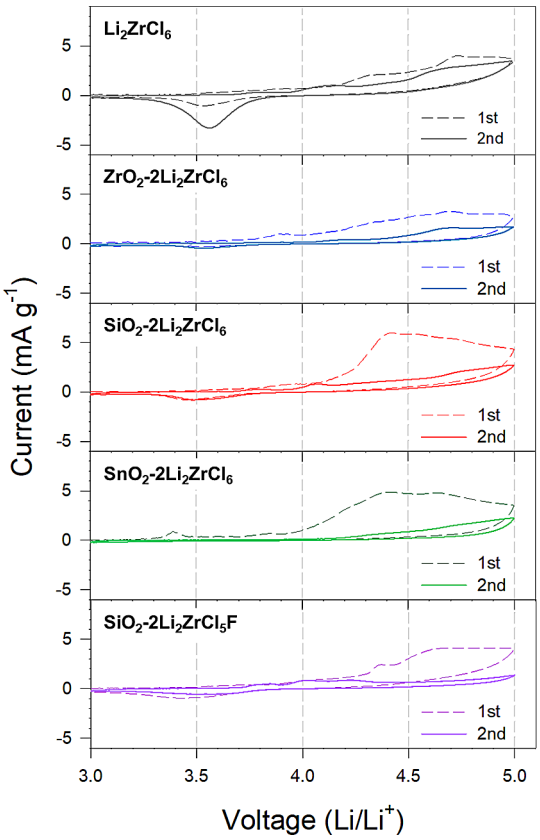

Figure 4. Electrochemical Stability of HNSEs. CV curves for (SE-C)|Li_6PS_5Cl|(Li−In) cells between 3.0 and 5.0 V (vs Li/Li^+) at 0.1 mV s^{-1} and 30 °C.

Li_3PO_4 (1 or 2 nm thick) using atomic layer deposition between Li_3InCl_6 and Li_6PS_5Cl. In this context, the metal or nonmetal oxides present at the HNSEs/Li_6PS_5Cl interface are assumed to affect the passivating behavior.

To enhance the compatibility with sulfide SEs, an F-substituted HNSE $SiO_2-2Li_2ZrCl_5F$ was synthesized by the mechanochemical milling of a 4LiCl−SiO_2, ZrF_4, and $ZrCl_4$ mixture. The XRD pattern of the $SiO_2-2Li_2ZrCl_5F$ HNSE revealed a small positive shift in the (301) peak at approximately 32° (Figure 5a), confirming successful fluorination of the Li_2ZrCl_6 domain. This fluorination process reduced the Li^+ conductivity from 0.47 to 0.26 mS cm^{-1} (Figure 5b), a value marginally lower than that of Li_2ZrCl_6. Furthermore, $SiO_2-2Li_2ZrCl_5F$ displayed a relatively higher integrated current of 3.01 mA V g^{-1} (~5.0 V vs Li/Li^+) at the initial cycle, followed by a remarkably lower integrated anodic current of 0.95 mA V g^{-1} in the second cycle (Figure 4), even when compared to $SiO_2-2Li_2ZrCl_6$ (1.53 mA V g^{-1}). According to DFT calculations, the enhanced electrochemical stability of $SiO_2-2Li_2ZrCl_5F$ is likely due to the formation of beneficial F-based passivating materials (Li_2ZrF_6 and $Li_3Zr_4F_{19}$).[59]

$SiO_2-2Li_2ZrCl_6$ and $SiO_2-2Li_2ZrCl_5F$ (hereafter referred to as SiO_2−LZC and SiO_2−LZCF, respectively) were evaluated in combination with uncoated $LiCoO_2$ electrodes in $LiCoO_2$|Li_6PS_5Cl|(Li−In) ASSB cells at 60 °C, a condition under which the incompatibility effect between halide and sulfide SEs was pronounced.[59,61,72,73] These results were compared with those obtained using Li_2ZrCl_6 (hereafter referred to as LZC), as shown in Figure 6. Figure 6a shows the initial charge−

https://doi.org/10.1021/acsami.4c08915
ACS Appl. Mater. Interfaces 2024, 16, 49328−49336

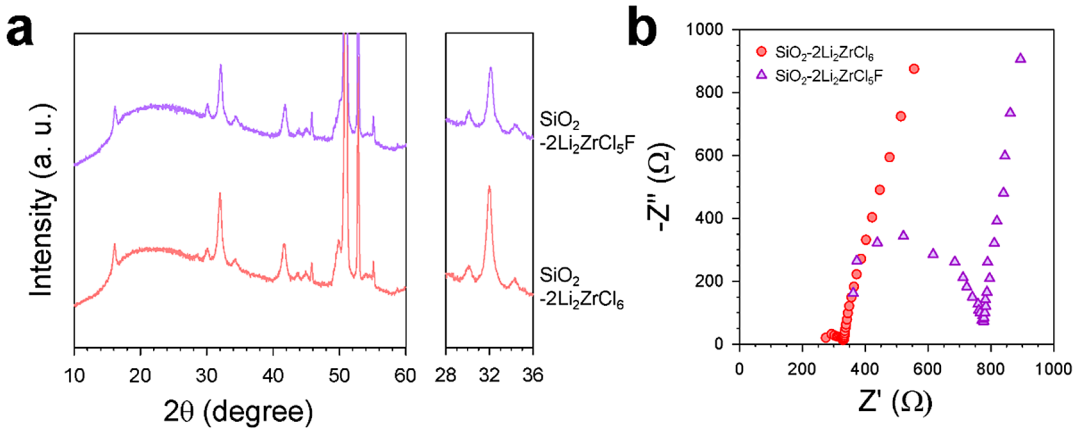

Figure 5. Characterization for F-substituted HNSEs. (a) XRD patterns and (b) Nyquist plots of Ti|HNSE|Ti symmetric cells for SiO_2−$2Li_2ZrCl_6$ and SiO_2−$2Li_2ZrCl_5F$.

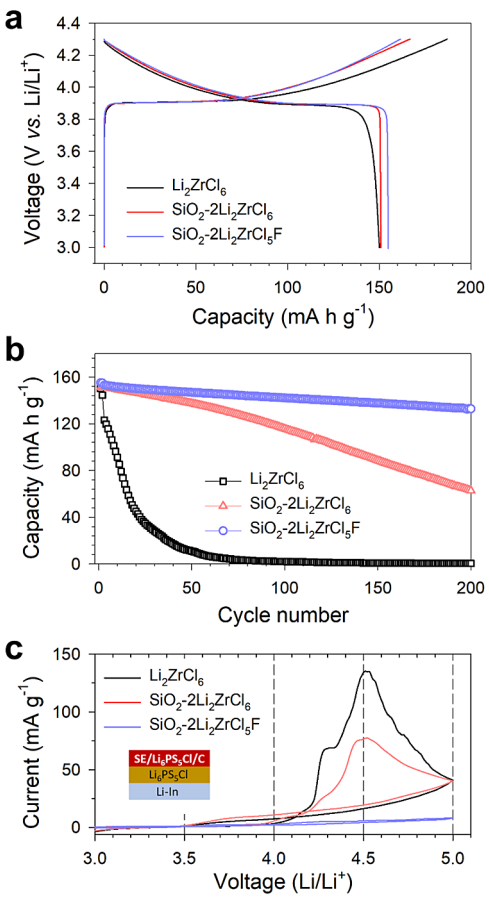

Figure 6. Electrochemical characterization of $LiCoO_2$||(Li−In) ASSBs employing LZC, SiO_2−LZC, and SiO_2−LZCF at 60 °C. (a) First-cycle charge−discharge voltage profiles at 0.1C for $LiCoO_2$ electrodes using LZC, SiO_2−LZC, and SiO_2−LZCF and (b) corresponding cycling performances at 0.5C. (c) CV curves for (halide SE-sulfide SE-C)|Li_6PS_5Cl||(Li−In) cells between 3.0 and 5.0 V (vs Li/Li^+) at 0.1 mV s^{-1} and 60 °C.

discharge at 0.1C (16 mA g^{-1}) voltage profiles for the $LiCoO_2$ electrodes employing LZC, SiO_2−LZC, and SiO_2−LZCF. A noticeable polarization was observed in the voltage profiles with LZC, leading to a reduced discharge capacity of 127 mA h g^{-1} and a low initial Coulombic efficiency (ICE) of 86.2%. In contrast, $LiCoO_2$ electrodes using SiO_2−LZC and SiO_2−LZCF demonstrated higher initial discharge capacities of 156 and 162 mA h g^{-1}, respectively, along with improved ICEs of 91.4 and 90.5%. The disparity in cycling performance was notable, following the descending order of SiO_2−LZCF > SiO_2−LZC ≫ LZC (Figure 6b), with capacity retentions at the 100th cycle being 93.7, 68.0, and 1.7%, respectively. The poor cycling performance of the ASSBs using LZC could be attributed to its incompatibility with the LCO and the sulfide SE employed as the separating SE layer. According to previous studies, common oxide compounds (SiO_2, ZrO_2, and SnO_2) exhibit stability when in contact with $Li_{0.5}CoO_2$.[74] Moreover, minor reactions between these oxides and the cathode can favorably introduce lithium into the oxides, enhancing Li-ion transport within the system (Figure S2, Table S1).[74] The superior capacity retention observed with SiO_2−LZC and SiO_2−LZCF indicates enhanced compatibility, which is attributed to integrating the oxide SiO_2 and fluorination.[38,74]

To investigate the compatibility of halide and sulfide SEs at 60 °C, a control experiment was devised with electrodes fabricated by manually blending SE powders (LZC, SiO_2−LZC, or SiO_2−LZCF), Li_6PS_5Cl, and super C65 in a weight ratio of 33.6:26.4:6. These electrodes were subjected to CV measurements ranging from 3.0 to 5.0 V (vs Li/Li^+) at a scan rate of 0.1 mV s^{-1} in Figure 6c. During the initial cycle, the LZC-Li_6PS_5Cl mixture electrode showed a substantial integrated anodic current of 88.9 mA V g^{-1} (∼5.0 V vs Li/Li^+), surpassing the anodic current of LZC alone and suggesting pronounced side reactions at the interface of carbon, LZC, and Li_6PS_5Cl. While the SiO_2−LZC−Li_6PS_5Cl mixture electrode showed a mitigated integrated anodic current of 71.6 mA V g^{-1} compared to the LZC−Li_6PS_5Cl electrode, it remained elevated. However, the utilization of SiO_2−LZCF significantly lowered the integrated anodic current to 12.8 mA V g^{-1}. The excellent compatibility between SiO_2−LZCF and Li_6PS_5Cl is validated by the ex situ X-ray photoelectron spectroscopy (XPS) result (Figure S6). The signal indicating the decomposition products of Zr−P−S species,[75] which results from a side reaction between halide and sulfide SEs, was pronounced in electrodes employing LZC and SiO_2−LZC. However, in electrodes that utilized SiO_2−LZCF, the presence of the Zr−P−S signal was notably lower. These findings align with the cycling performance data of the LCO electrodes (Figure 6b) and underscore the positive effect of an F-based passivating layer.

https://doi.org/10.1021/acsami.4c08915
ACS Appl. Mater. Interfaces 2024, 16, 49328−49336

Moreover, the high-voltage stabilities of LCO electrodes with SiO_2−LZCF were evaluated in ASSB cells at 60 °C, demonstrating stability up to 4.5 V (vs Li/Li^+) (Figure S7). Employing SiO_2−LZCF, the discharge capacity exhibited 184 mA h g^{-1} with an exceptional ICE of 95.5%. However, this cell showed inferior cycling performance at the higher cutoff voltage of 4.5 V (71.4% retention) compared to 93.7% for a lower cutoff voltage of 4.3 V. This difference could originate from both the inherent structural instability of LCO at elevated voltages and the limited electrochemical oxidative stability of the SiO_2−LZCF,[37,38,76−78] indicating a need for further advancements.

3. CONCLUSIONS

In summary, halide nanocomposite superionic conductors incorporating various metal or nonmetal oxides, MO_2−$2Li_2ZrCl_6$ (M = Zr, Si, or Sn), were synthesized via a two-step mechanochemical process. Despite incorporating ionically insulating metal or nonmetal oxide phases into the HNSEs, they all demonstrated ionic conductivities surpassing those of Li_2ZrCl_6, highlighting the effect of the promoted interfacial superionic conduction. Furthermore, the incorporation of SiO_2 into Li_2ZrCl_6 to form SiO_2−$2Li_2ZrCl_6$ HNSE markedly decreases the specific density while preserving the enhanced Li^+ conductivity—a critical factor for the high energy density required in ASSB cells. In the hybrid configuration of halide-sulfide SE systems in ASSBs, both the oxide in the HNSEs and the fluorination mitigated the incompatibility between the two materials, owing to the enhanced passivation between the halide and sulfide interfaces. Finally, the HNSEs, particularly the F-substituted HNSE, SiO_2−$2Li_2ZrCl_5F$, demonstrated outstanding electrochemical energy storage performances in $LiCoO_2$|Li_6PS_5Cl|(Li−In) ASSB cells at 60 °C, as evidenced by their capacity, ICE, and cycling performance, which align with the CV and ex situ XPS results. These findings highlight the potential of leveraging unique interfacial effects to optimize the superionic conduction, (electro)chemical stability, and density, thereby offering invaluable insights into designing advanced superionic conductors for practical applications.

4. EXPERIMENTAL SECTION

4.1. Preparation of Materials. A stoichiometric mixture of Li_2O (99.5%, Alfa Aesar) and $ZrCl_4$ (99.99%, Sigma-Aldrich), $SiCl_4$ (99.998%, Sigma-Aldrich), or $SnCl_4$ (99.99%, Alfa Aesar) was ball-milled at 600 rpm for 20 h in a ZrO_2 vial with ZrO_2 balls using the Pulverisette 7PL (Fritsch GmbH) to synthesize 4LiCl-MO_2 (M = Zr, Si, or Sn). For the synthesis of HNSE MO_2-$2Li_2ZrCl_6$ (M = Zr, Si, or Sn), 4LiCl-MO_2 (M = Zr, Si, or Sn) was mixed with $ZrCl_4$ (99.99%, Sigma-Aldrich) in stoichiometric proportions and ball-milled under the same conditions as those used for the conventional HNSEs. To synthesize Li_6PS_5Cl, a stoichiometric blend of Li_2S (99.9%, Alfa Aesar), P_2S_5 (99%, Sigma-Aldrich), and LiCl (99.99%, Sigma-Aldrich) was ball-milled at 600 rpm for 10 h in a ZrO_2 vial with ZrO_2 balls. This was followed by annealing at 550 °C under an Ar atmosphere for 6 h.

4.2. Material Characterization. Using a Rigaku MiniFlex600 diffractometer with Cu Kα radiation (λ = 1.5406 Å) at 40 kV and 15 mA, XRD patterns of the powder samples were collected. The XRD cells, which held hermetically sealed samples with a Be window, were mounted on the diffractometer. At the National Synchrotron Light Source II (NSLSII) at Brookhaven National Laboratory, X-ray total-scattering data were obtained at the 28-ID-1 PDF beamline using an X-ray energy of 74.5 keV (λ = 0.1665 Å), with the samples contained in polyimide (Kapton) tubes and sealed with epoxy resin. Using Dioptas software[79] with CeO_2 as a calibrant, the 2D images were converted to a 1D pattern, and the PDF $G(r)$ was obtained from Fourier transformation with a Q range of 0.1−22 $Å^{-1}$ using xPDFsuite.[80] Using an AURIGA (Carl Zeiss) microscope, FESEM images and corresponding EDX elemental maps were obtained. To avoid exposure to ambient air, the sample specimens were stored and transported in an air isolation system holder. Measured by the Archimedes method using Dibromomethane, the relative densities of the samples were determined.[43]

4.3. Electrochemical Characterization. The AC impedance method was used to measure ionic conductivities with ion-blocking Ti|SE|Ti symmetric cells. Cold-pressed pellets (6 mm in diameter and prepared at 370 MPa) were tested under an external pressure of approximately 70 MPa at an open circuit voltage. Using a VSP-300 (Bio-Logic), EIS data were collected with an amplitude of 10 mV over a frequency range of 10 mHz to 7 MHz, recording ten data points per frequency decade. In the all-solid-state half-cells, the counter and reference electrodes were Li−In. Prepared by ball-milling In (Aldrich, 99%) and Li (FMC Lithium Corp.) to achieve a nominal composition of $Li_{0.5}In$, these powders were then mixed with Li_6PS_5Cl powders in an 8:2 weight ratio. Different types of SE powders (Li_2ZrCl_6, ZrO_2-$2Li_2ZrCl_6$, SnO_2-$2Li_2ZrCl_6$, SiO_2-$2Li_2ZrCl_6$, and SiO_2-$2Li_2ZrCl_5F$) were manually mixed with super C65 in a 10:1 weight ratio for the CV measurements. Li_6PS_5Cl was pelletized under 100 MPa to form SE layers, which were then sandwiched between SE-super C65 mixtures and Li−In electrodes. After pressing the assembly at 370 MPa, the CV measurements were performed using a VMP3 (Bio-Logic) with a scan range of open-circuit voltage (OCV) to 5.0 V (vs Li/Li^+) with scan rate of 0.1 mV s^{-1}. All-solid-state cells were fabricated as follows. To prepare the Li_6PS_5Cl monolayer, Li_6PS_5Cl powders (150 mg, approximately 600 μm) were pelletized under 100 MPa, and a mixture of $LiCoO_2$, HNSEs, and super C65 powders in a 70:30:3 weight ratio were used to prepare composite working electrodes. A layer of cathode composite mixture, weighing 15 mg and corresponding to a theoretical areal capacity of 2.1 mA h cm^{-2}, was spread, while 65 mg of the anode composite mixture, with a theoretical areal capacity of 4.3 mA h cm^{-2}, was applied to the opposite side of the pellet and pressed at 370 MPa for 3 min. The capacity ratio of the anode and cathode is 2.0. After attaching the $LiCoO_2$ electrodes (40−50 μm) and the Li−In electrodes (∼130 μm) to either side of the SE layers, the entire assembly was pressed at 370 MPa. Tested under an external pressure of approximately 70 MPa, the solid-state cells were evaluated.

4.4. Computational Details. Using the Vienna Ab initio Simulation Package (VASP),[81] calculations were performed with the Generalized Gradient Approximation (GGA) exchange-correlation, employing the Perdew−Burke−Ernzerhof (PBE) functional.[82] The projector-augmented wave (PAW) method was used, and a plane-wave cutoff energy of 520 eV was applied. Additionally, each structure's cell shape, volume, and atomic positions underwent full relaxation until the forces on individual atoms reached below 0.05 eV/Å. The mutual pseudobinary reaction energy is calculated as

$$\Delta E_{r\times n}(C_A, C_B, x) = E_{eq}(xC_A + (1-x)C_B) - xE(C_A) - (1-x)E(C_B)$$

where x is the molar fraction of the material A with C_A and C_B which are the compositions of material A and material B, respectively.

The most stable convex hull energy, representing the lowest energy of phase equilibrium, was used for a given composition. The Materials Project database[83] provided the structures of all known compounds in the Li−M−O−Cl (M = Zr, Si, and Sn) systems, and their energies were computed using the same DFT calculation parameters.

■ ASSOCIATED CONTENT

Supporting Information

The Supporting Information is available free of charge at https://pubs.acs.org/doi/10.1021/acsami.4c08915.

https://doi.org/10.1021/acsami.4c08915
ACS Appl. Mater. Interfaces 2024, 16, 49328−49336

Experimental section, DFT calculation results, SEM and TEM images of solid electrolytes, equivalent circuit model, ex situ XPS spectra of halide SE-sulfide SE-carbon electrodes, and cycling performance of LCO electrodes at 4.5 V (PDF)

■ AUTHOR INFORMATION

Corresponding Author

Yoon Seok Jung − *Department of Chemical and Biomolecular Engineering and Department of Battery Engineering, Yonsei University, Seoul 03722, Republic of Korea;* orcid.org/0000-0003-0357-9508; Email: yoonsjung@yonsei.ac.kr

Authors

Hiram Kwak − *Department of Chemical and Biomolecular Engineering, Yonsei University, Seoul 03722, Republic of Korea*

Jong Seok Kim − *Department of Chemical and Biomolecular Engineering, Yonsei University, Seoul 03722, Republic of Korea*

Daseul Han − *Department of Energy and Materials Engineering, Dongguk University, Seoul 04620, Republic of Korea*

Jae-Seung Kim − *Department of Materials Science and Engineering, Korea Advanced Institute of Science and Technology (KAIST), Daejeon 34141, Republic of Korea;* orcid.org/0000-0003-3052-6444

Juhyoun Park − *Department of Chemical and Biomolecular Engineering, Yonsei University, Seoul 03722, Republic of Korea*

Changhoon Kim − *Department of Chemical and Biomolecular Engineering, Yonsei University, Seoul 03722, Republic of Korea*

Dong-Hwa Seo − *Department of Materials Science and Engineering, Korea Advanced Institute of Science and Technology (KAIST), Daejeon 34141, Republic of Korea*

Kyung-Wan Nam − *Department of Energy and Materials Engineering, Dongguk University, Seoul 04620, Republic of Korea;* orcid.org/0000-0001-6278-6369

Complete contact information is available at: https://pubs.acs.org/10.1021/acsami.4c08915

Notes

The authors declare no competing financial interest.

■ ACKNOWLEDGMENTS

This work was supported by the Samsung Research Funding & Incubation Center of Samsung Electronics under Project No. SRFC-MA2102-03. The PDF research used beamline 28-ID-1(PDF) of the National Synchrotron Light Source II, a US Department of Energy (DOE) Office of Science User Facility operated for the DOE Office of Science by Brookhaven National Laboratory under contract no. DE-SC0012704. The computational work was supported by the Supercomputing Center/Korea Institute of Science and Technology Information with supercomputing resources, including technical support (KSC-2023-CRE-0025 to D.-H.S.).

■ REFERENCES

(1) Choi, J. W.; Aurbach, D. Promise and reality of post-lithium-ion batteries with high energy densities. *Nat. Rev. Mater.* **2016**, *1* (4), No. 16013.

(2) Janek, J.; Zeier, W. G. A solid future for battery development. *Nat. Energy* **2016**, *1* (9), No. 16141.

(3) Manthiram, A.; Yu, X.; Wang, S. Lithium battery chemistries enabled by solid-state electrolytes. *Nat. Rev. Mater.* **2017**, *2* (4), No. 16103.

(4) Wang, M. J.; Kazyak, E.; Dasgupta, N. P.; Sakamoto, J. Transitioning solid-state batteries from lab to market: Linking electro-chemo-mechanics with practical considerations. *Joule* **2021**, *5* (6), 1371−1390.

(5) Duffner, F.; Kronemeyer, N.; Tübke, J.; Leker, J.; Winter, M.; Schmuch, R. Post-lithium-ion battery cell production and its compatibility with lithium-ion cell production infrastructure. *Nat. Energy* **2021**, *6* (2), 123−134.

(6) Song, Y. B.; Baeck, K. H.; Kwak, H.; Lim, H.; Jung, Y. S. Dimensional Strategies for Bridging the Research Gap between Lab-Scale and Potentially Practical All-Solid-State Batteries: The Role of Sulfide Solid Electrolyte Films. *Adv. Energy Mater.* **2023**, *13* (32), No. 2301142.

(7) Park, K. H.; Bai, Q.; Kim, D. H.; Oh, D. Y.; Zhu, Y.; Mo, Y.; Jung, Y. S. Design strategies, practical considerations, and new solution processes of sulfide solid electrolytes for all-solid-state batteries. *Adv. Energy Mater.* **2018**, *8* (18), No. 1800035.

(8) Kamaya, N.; Homma, K.; Yamakawa, Y.; Hirayama, M.; Kanno, R.; Yonemura, M.; Kamiyama, T.; Kato, Y.; Hama, S.; Kawamoto, K.; Mitsui, A. A lithium superionic conductor. *Nat. Mater.* **2011**, *10* (9), 682−686.

(9) Chen, S.; Xie, D.; Liu, G.; Mwizerwa, J. P.; Zhang, Q.; Zhao, Y.; Xu, X.; Yao, X. Sulfide solid electrolytes for all-solid-state lithium batteries: Structure, conductivity, stability and application. *Energy Storage Mater.* **2018**, *14*, 58−74.

(10) Cheng, X.-B.; Zhang, R.; Zhao, C.-Z.; Zhang, Q. Toward Safe Lithium Metal Anode in Rechargeable Batteries: A Review. *Chem. Rev.* **2017**, *117* (15), 10403−10473.

(11) Han, X.; Gong, Y.; Fu, K.; He, X.; Hitz, G. T.; Dai, J.; Pearse, A.; Liu, B.; Wang, H.; Rubloff, G.; Mo, Y.; Thangadurai, V.; Wachsman, E. D.; Hu, L. Negating interfacial impedance in garnet-based solid-state Li metal batteries. *Nat. Mater.* **2017**, *16* (5), 572−579.

(12) Hayashi, A.; Noi, K.; Sakuda, A.; Tatsumisago, M. Superionic glass-ceramic electrolytes for room-temperature rechargeable sodium batteries. *Nat. Commun.* **2012**, *3* (1), 856.

(13) Thangadurai, V.; Narayanan, S.; Pinzaru, D. Garnet-type solid-state fast Li ion conductors for Li batteries: critical review. *Chem. Soc. Rev.* **2014**, *43* (13), 4714−4727.

(14) Zhang, Z.; Shao, Y.; Lotsch, B.; Hu, Y.-S.; Li, H.; Janek, J.; Nazar, L. F.; Nan, C.-W.; Maier, J.; Armand, M.; Chen, L. New horizons for inorganic solid state ion conductors. *Energy Environ. Sci.* **2018**, *11* (8), 1945−1976.

(15) Han, Y.; Jung, S. H.; Kwak, H.; Jun, S.; Kwak, H. H.; Lee, J. H.; Hong, S.-T.; Jung, Y. S. Single- or Poly-Crystalline Ni-Rich Layered Cathode, Sulfide or Halide Solid Electrolyte: Which Will be the Winners for All-Solid-State Batteries? *Adv. Energy Mater.* **2021**, *11* (21), No. 2100126.

(16) Li, X.; Liang, J.; Yang, X.; Adair, K. R.; Wang, C.; Zhao, F.; Sun, X. Progress and perspectives on halide lithium conductors for all-solid-state lithium batteries. *Energy Environ. Sci.* **2020**, *13* (5), 1429−1461.

(17) Kwak, H.; Wang, S.; Park, J.; Liu, Y.; Kim, K. T.; Choi, Y.; Mo, Y.; Jung, Y. S. Emerging Halide Superionic Conductors for All-Solid-State Batteries: Design, Synthesis, and Practical Applications. *ACS Energy Lett.* **2022**, *7* (5), 1776−1805.

(18) Ye, L.; Li, X. A dynamic stability design strategy for lithium metal solid state batteries. *Nature* **2021**, *593* (7858), 218−222.

(19) Tan, D. H. S.; Chen, Y.-T.; Yang, H.; Bao, W.; Sreenarayanan, B.; Doux, J.-M.; Li, W.; Lu, B.; Ham, S.-Y.; Sayahpour, B.; Scharf, J.; Wu, E. A.; Deysher, G.; Han, H. E.; Hah, H. J.; Jeong, H.; Lee, J. B.; Chen, Z.; Meng, Y. S. Carbon-free high-loading silicon anodes enabled by sulfide solid electrolytes. *Science* **2021**, *373* (6562), 1494−1499.

(20) Jun, S.; Lee, G.; Song, Y. B.; Lim, H.; Baeck, K. H.; Lee, E. S.; Kim, J. Y.; Kim, D. W.; Park, J. H.; Jung, Y. S. Interlayer Engineering and Prelithiation: Empowering Si Anodes for Low-Pressure-Operating All-Solid-State Batteries. *Small* **2024**, *20* (25), No. 2309437.
(21) Lim, H.; Jun, S.; Song, Y. B.; Baeck, K. H.; Bae, H.; Lee, G.; Kim, J.; Jung, Y. S. Rationally Designed Conversion-Type Lithium Metal Protective Layer for All-Solid-State Lithium Metal Batteries. *Adv. Energy Mater.* **2024**, *14* (12), No. 2303762.
(22) Wu, J.; Liu, S.; Han, F.; Yao, X.; Wang, C. Lithium/Sulfide All-Solid-State Batteries using Sulfide Electrolytes. *Adv. Mater.* **2021**, *33* (6), No. 2000751.
(23) Deiseroth, H. J.; Kong, S. T.; Eckert, H.; Vannahme, J.; Reiner, C.; Zaiß, T.; Schlosser, M. Li_6PS_5X: a class of crystalline Li-rich solids with an unusually high Li^+ mobility. *Angew. Chem., Int. Ed.* **2008**, *120* (4), 767−770.
(24) Zhou, L.; Minafra, N.; Zeier, W. G.; Nazar, L. F. Innovative Approaches to Li-Argyrodite Solid Electrolytes for All-Solid-State Lithium Batteries. *Acc. Chem. Res.* **2021**, *54* (12), 2717−2728.
(25) Zhu, Y.; He, X.; Mo, Y. Origin of Outstanding Stability in the Lithium Solid Electrolyte Materials: Insights from Thermodynamic Analyses Based on First-Principles Calculations. *ACS Appl. Mater. Interfaces* **2015**, *7* (42), 23685−23693.
(26) Sakuda, A.; Hayashi, A.; Tatsumisago, M. Interfacial observation between $LiCoO_2$ electrode and $Li_2S-P_2S_5$ solid electrolytes of all-solid-state lithium secondary batteries using transmission electron microscopy. *Chem. Mater.* **2010**, *22* (3), 949−956.
(27) Xiao, Y.; Wang, Y.; Bo, S.-H.; Kim, J. C.; Miara, L. J.; Ceder, G. Understanding interface stability in solid-state batteries. *Nat. Rev. Mater.* **2020**, *5* (2), 105−126.
(28) Jang, B.; Woo, J.; Song, Y. B.; Kwak, H.; Park, J.; Kim, J. S.; Lim, H.; Jung, Y. S. Microwave heating enables near-carbonless liquid-phase-derived Li Argyrodites for all-solid-state batteries. *Energy Storage Mater.* **2024**, *65*, No. 103154.
(29) Chen, S.; Xie, D.; Liu, G.; Mwizerwa, J. P.; Zhang, Q.; Zhao, Y.; Xu, X.; Yao, X. Sulfide solid electrolytes for all-solid-state lithium batteries: Structure, conductivity, stability and application. *Energy Storage Mater.* **2018**, *14*, 58−74.
(30) Jung, S. H.; Oh, K.; Nam, Y. J.; Oh, D. Y.; Brüner, P.; Kang, K.; Jung, Y. S. $Li_3BO_3-Li_2CO_3$: Rationally Designed Buffering Phase for Sulfide All-Solid-State Li-Ion Batteries. *Chem. Mater.* **2018**, *30* (22), 8190−8200.
(31) Wang, K.; Liang, Z.; Weng, S.; Ding, Y.; Su, Y.; Wu, Y.; Zhong, H.; Fu, A.; Sun, Y.; Luo, M.; Yan, J.; Wang, X.; Yang, Y. Surface Engineering Strategy Enables 4.5 V Sulfide-Based All-Solid-State Batteries with High Cathode Loading and Long Cycle Life. *ACS Energy Lett.* **2023**, *8* (8), 3450−3459.
(32) Wu, J.; Shen, L.; Zhang, Z.; Liu, G.; Wang, Z.; Zhou, D.; Wan, H.; Xu, X.; Yao, X. All-Solid-State Lithium Batteries with Sulfide Electrolytes and Oxide Cathodes. *Electrochemical Energy Reviews* **2021**, *4* (1), 101−135.
(33) Stramare, S.; Thangadurai, V.; Weppner, W. Lithium lanthanum titanates: a review. *Chem. Mater.* **2003**, *15* (21), 3974−3990.
(34) Kim, S.; Kim, J.-S.; Miara, L.; Wang, Y.; Jung, S.-K.; Park, S. Y.; Song, Z.; Kim, H.; Badding, M.; Chang, J.; Roev, V.; Yoon, G.; Kim, R.; Kim, J.-H.; Yoon, K.; Im, D.; Kang, K. High-energy and durable lithium metal batteries using garnet-type solid electrolytes with tailored lithium-metal compatibility. *Nat. Commun.* **2022**, *13* (1), 1883.
(35) Kim, K. H.; Iriyama, Y.; Yamamoto, K.; Kumazaki, S.; Asaka, T.; Tanabe, K.; Fisher, C. A. J.; Hirayama, T.; Murugan, R.; Ogumi, Z. Characterization of the interface between $LiCoO_2$ and $Li_7La_3Zr_2O_{12}$ in an all-solid-state rechargeable lithium battery. *J. Power Sources* **2011**, *196* (2), 764−767.
(36) Asano, T.; Sakai, A.; Ouchi, S.; Sakaida, M.; Miyazaki, A.; Hasegawa, S. Solid Halide Electrolytes with High Lithium-Ion Conductivity for Application in 4 V Class Bulk-Type All-Solid-State Batteries. *Adv. Mater.* **2018**, *30* (44), No. 1803075.
(37) Kim, K.; Park, D.; Jung, H.-G.; Chung, K. Y.; Shim, J. H.; Wood, B. C.; Yu, S. Material Design Strategy for Halide Solid Electrolytes Li_3MX_6 (X = Cl, Br, and I) for All-Solid-State High-Voltage Li-Ion Batteries. *Chem. Mater.* **2021**, *33* (10), 3669−3677.
(38) Wang, S.; Bai, Q.; Nolan, A. M.; Liu, Y.; Gong, S.; Sun, Q.; Mo, Y. Lithium Chlorides and Bromides as Promising Solid-State Chemistries for Fast Ion Conductors with Good Electrochemical Stability. *Angew. Chem., Int. Ed.* **2019**, *58* (24), 8039−8043.
(39) Li, X.; Liang, J.; Luo, J.; Norouzi Banis, M.; Wang, C.; Li, W.; Deng, S.; Yu, C.; Zhao, F.; Hu, Y.; Sham, T.-K.; Zhang, L.; Zhao, S.; Lu, S.; Huang, H.; Li, R.; Adair, K. R.; Sun, X. Air-stable Li_3InCl_6 electrolyte with high voltage compatibility for all-solid-state batteries. *Energy Environ. Sci.* **2019**, *12* (9), 2665−2671.
(40) Liang, J.; Li, X.; Wang, S.; Adair, K. R.; Li, W.; Zhao, Y.; Wang, C.; Hu, Y.; Zhang, L.; Zhao, S.; Lu, S.; Huang, H.; Li, R.; Mo, Y.; Sun, X. Site-Occupation-Tuned Superionic Li_xScCl_{3+x}Halide Solid Electrolytes for All-Solid-State Batteries. *J. Am. Chem. Soc.* **2020**, *142* (15), 7012−7022.
(41) Zhou, L.; Kwok, C. Y.; Shyamsunder, A.; Zhang, Q.; Wu, X.; Nazar, L. F. A new halospinel superionic conductor for high-voltage all solid state lithium batteries. *Energy Environ. Sci.* **2020**, *13* (7), 2056−2063.
(42) Kim, S. Y.; Kaup, K.; Park, K.-H.; Assoud, A.; Zhou, L.; Liu, J.; Wu, X.; Nazar, L. F. Lithium Ytterbium-Based Halide Solid Electrolytes for High Voltage All-Solid-State Batteries. *ACS Mater. Lett.* **2021**, *3*, 930−938.
(43) Kwak, H.; Han, D.; Lyoo, J.; Park, J.; Jung, S. H.; Han, Y.; Kwon, G.; Kim, H.; Hong, S.-T.; Nam, K.-W.; Jung, Y. S. New Cost-Effective Halide Solid Electrolytes for All-Solid-State Batteries: Mechanochemically Prepared Fe^{3+}-Substituted Li_2ZrCl_6. *Adv. Energy Mater.* **2021**, *11* (12), No. 2003190.
(44) Ishiguro, Y.; Ueno, K.; Nishimura, S.; Iida, G.; Igarashib, Y. $TaCl_5$-glassified Ultrafast Lithium Ion-conductive Halide Electrolytes for High-performance All-solid-state Lithium Batteries. *Chem. Lett.* **2023**, *52* (4), 237−241.
(45) Tanaka, Y.; Ueno, K.; Mizuno, K.; Takeuchi, K.; Asano, T.; Sakai, A. New Oxyhalide Solid Electrolytes with High Lithium Ionic Conductivity > 10 mS cm^{-1} for All-Solid-State Batteries. *Angew. Chem., Int. Ed.* **2023**, *62* (13), No. e202217581.
(46) Zhang, S.; Zhao, F.; Chen, J.; Fu, J.; Luo, J.; Alahakoon, S. H.; Chang, L.-Y.; Feng, R.; Shakouri, M.; Liang, J.; Zhao, Y.; Li, X.; He, L.; Huang, Y.; Sham, T.-K.; Sun, X. A family of oxychloride amorphous solid electrolytes for long-cycling all-solid-state lithium batteries. *Nat. Commun.* **2023**, *14* (1), 3780.
(47) Jun, K.; Sun, Y.; Xiao, Y.; Zeng, Y.; Kim, R.; Kim, H.; Miara, L. J.; Im, D.; Wang, Y.; Ceder, G. Lithium superionic conductors with corner-sharing frameworks. *Nat. Mater.* **2022**, *21* (8), 924−931.
(48) Fu, J.; Wang, S.; Liang, J.; Alahakoon, S. H.; Wu, D.; Luo, J.; Duan, H.; Zhang, S.; Zhao, F.; Li, W.; Li, M.; Hao, X.; Li, X.; Chen, J.; Chen, N.; King, G.; Chang, L.-Y.; Li, R.; Huang, Y.; Gu, M.; Sham, T.-K.; Mo, Y.; Sun, X. Superionic Conducting Halide Frameworks Enabled by Interface-Bonded Halides. *J. Am. Chem. Soc.* **2023**, *145* (4), 2183−2194.
(49) Yin, Y.-C.; Yang, J.-T.; Luo, J.-D.; Lu, G.-X.; Huang, Z.; Wang, J.-P.; Li, P.; Li, F.; Wu, Y.-C.; Tian, T.; Meng, Y.-F.; Mo, H.-S.; Song, Y.-H.; Yang, J.-N.; Feng, L.-Z.; Ma, T.; Wen, W.; Gong, K.; Wang, L.-J.; Ju, H.-X.; Xiao, Y.; Li, Z.; Tao, X.; Yao, H.-B. A $LaCl_3$-based lithium superionic conductor compatible with lithium metal. *Nature* **2023**, *616* (7955), 77−83.
(50) Kato, Y.; Hori, S.; Saito, T.; Suzuki, K.; Hirayama, M.; Mitsui, A.; Yonemura, M.; Iba, H.; Kanno, R. High-power all-solid-state batteries using sulfide superionic conductors. *Nat. Energy* **2016**, *1* (4), No. 16030.
(51) Kwak, H.; Han, D.; Son, J. P.; Kim, J. S.; Park, J.; Nam, K.-W.; Kim, H.; Jung, Y. S. Li^+ conduction in aliovalent-substituted monoclinic Li_2ZrCl_6 for all-solid-state batteries: $Li_{2+x}Zr_{1-x}M_xCl_6$ (M = In, Sc). *Chem. Eng. J.* **2022**, *437*, No. 135413.

https://doi.org/10.1021/acsami.4c08915
ACS Appl. Mater. Interfaces 2024, 16, 49328−49336

(52) Park, K.-H.; Kaup, K.; Assoud, A.; Zhang, Q.; Wu, X.; Nazar, L. F. High-Voltage Superionic Halide Solid Electrolytes for All-Solid-State Li-Ion Batteries. *ACS Energy Lett.* **2020**, *5* (2), 533−539.
(53) Liu, Z.; Ma, S.; Liu, J.; Xiong, S.; Ma, Y.; Chen, H. High Ionic Conductivity Achieved in $Li_3Y(Br_3Cl_3)$ Mixed Halide Solid Electrolyte via Promoted Diffusion Pathways and Enhanced Grain Boundary. *ACS Energy Lett.* **2021**, *6* (1), 298−304.
(54) Wu, E. A.; Banerjee, S.; Tang, H.; Richardson, P. M.; Doux, J.-M.; Qi, J.; Zhu, Z.; Grenier, A.; Li, Y.; Zhao, E.; Deysher, G.; Sebti, E.; Nguyen, H.; Stephens, R.; Verbist, G.; Chapman, K. W.; Clément, R. J.; Banerjee, A.; Meng, Y. S.; Ong, S. P. A stable cathode-solid electrolyte composite for high-voltage, long-cycle-life solid-state sodium-ion batteries. *Nat. Commun.* **2021**, *12* (1), 1256.
(55) Park, J.; Han, D.; Kwak, H.; Han, Y.; Choi, Y. J.; Nam, K.-W.; Jung, Y. S. Heat treatment protocol for modulating ionic conductivity via structural evolution of $Li_{3-x}Yb_{1-x}M_xCl_6$ (M = Hf^{4+}, Zr^{4+}) new halide superionic conductors for all-solid-state batteries. *Chem. Eng. J.* **2021**, *425*, No. 130630.
(56) Schlem, R.; Muy, S.; Prinz, N.; Banik, A.; Shao-Horn, Y.; Zobel, M.; Zeier, W. G. Mechanochemical Synthesis: A Tool to Tune Cation Site Disorder and Ionic Transport Properties of Li_3MCl_6 (M = Y, Er) Superionic Conductors. *Adv. Energy Mater.* **2020**, *10* (6), No. 1903719.
(57) Sebti, E.; Evans, H. A.; Chen, H.; Richardson, P. M.; White, K. M.; Giovine, R.; Koirala, K. P.; Xu, Y.; Gonzalez-Correa, E.; Wang, C.; Brown, C. M.; Cheetham, A. K.; Canepa, P.; Clément, R. J. Stacking Faults Assist Lithium-Ion Conduction in a Halide-Based Superionic Conductor. *J. Am. Chem. Soc.* **2022**, *144* (13), 5795−5811.
(58) Yu, S.; Noh, J.; Kim, B.; Song, J.-H.; Oh, K.; Yoo, J.; Lee, S.; Park, S.-O.; Kim, W.; Kang, B.; Kil, D.; Kang, K. Design of a trigonal halide superionic conductor by regulating cation order-disorder. *Science* **2023**, *382* (6670), 573−579.
(59) Kwak, H.; Kim, J.-S.; Han, D.; Kim, J. S.; Park, J.; Kwon, G.; Bak, S.-M.; Heo, U.; Park, C.; Lee, H.-W.; Nam, K.-W.; Seo, D.-H.; Jung, Y. S. Boosting the interfacial superionic conduction of halide solid electrolytes for all-solid-state batteries. *Nat. Commun.* **2023**, *14* (1), 2459.
(60) Park, J.; Han, D.; Son, J. P.; Kwak, H.; Ko, W.; Park, C.; Lee, C.; Lee, H.-W.; Kim, J.; Nam, K.-W.; Jung, Y. S. Extending the Electrochemical Window of Na^+ Halide Nanocomposite Solid Electrolytes for 5 V-Class All-Solid-State Na-Ion Batteries. *ACS Energy Lett.* **2024**, *9* (5), 2222−2230.
(61) Koç, T.; Hallot, M.; Quemin, E.; Hennequart, B.; Dugas, R.; Abakumov, A. M.; Lethien, C.; Tarascon, J.-M. Toward Optimization of the Chemical/Electrochemical Compatibility of Halide Solid Electrolytes in All-Solid-State Batteries. *ACS Energy Lett.* **2022**, *7* (9), 2979−2987.
(62) Isobe, H.; Kaneko, K. Porous Silica Particles Prepared from Silicon Tetrachloride Using Ultrasonic Spray Method. *J. Colloid Interface Sci.* **1999**, *212* (2), 234−241.
(63) Park, H. K.; Park, K. Y. Vapor-phase synthesis of uniform silica spheres through two-stage hydrolysis of $SiCl_4$. *Mater. Res. Bull.* **2008**, *43* (11), 2833−2839.
(64) Yan, F.; Jiang, J.; Chen, X.; Tian, S.; Li, K. Synthesis and Characterization of Silica Nanoparticles Preparing by Low-Temperature Vapor-Phase Hydrolysis of $SiCl_4$. *Ind. Eng. Chem. Res.* **2014**, *53* (30), 11884−11890.
(65) Ching, W. Y. Theory of amorphous SiO_2 and SiO_x. II. Electron states in an intrinsic glass. *Phys. Rev. B* **1982**, *26* (12), 6622−6632.
(66) Hoang, V. V. Molecular Dynamics Simulation of Amorphous SiO_2 Nanoparticles. *J. Phys. Chem. B* **2007**, *111* (44), 12649−12656.
(67) Li, N.; Ching, W.-Y. Structural, electronic and optical properties of a large random network model of amorphous SiO_2 glass. *J. Non-Cryst. Solids* **2014**, *383*, 28−32.
(68) Li, C.; Gu, L.; Maier, J. Enhancement of the Li Conductivity in LiF by Introducing Glass/Crystal Interfaces. *Adv. Funct. Mater.* **2012**, *22* (6), 1145−1149.
(69) Sata, N.; Eberman, K.; Eberl, K.; Maier, J. Mesoscopic fast ion conduction in nanometre-scale planar heterostructures. *Nature* **2000**, *408* (6815), 946−949.
(70) Liang, C. C. Conduction Characteristics of the Lithium Iodide-Aluminum Oxide Solid Electrolytes. *J. Electrochem. Soc.* **1973**, *120* (10), 1289.
(71) Kim, J. S.; Jung, S.; Kwak, H.; Han, Y.; Kim, S.; Lim, J.; Lee, Y. M.; Jung, Y. S. Synergistic halide-sulfide hybrid solid electrolytes for Ni-rich cathodes design guided by digital twin for all-solid-State Li batteries. *Energy Storage Mater.* **2023**, *55*, 193−204.
(72) Rosenbach, C.; Walther, F.; Ruhl, J.; Hartmann, M.; Hendriks, T. A.; Ohno, S.; Janek, J.; Zeier, W. G. Visualizing the Chemical Incompatibility of Halide and Sulfide-Based Electrolytes in Solid-State Batteries. *Adv. Energy Mater.* **2023**, *13* (6), No. 2203673.
(73) Koç, T.; Marchini, F.; Rousse, G.; Dugas, R.; Tarascon, J.-M. In Search of the Best Solid Electrolyte-Layered Oxide Pairing for Assembling Practical All-Solid-State Batteries. *ACS Appl. Energy Mater.* **2021**, *4* (12), 13575−13585.
(74) Nolan, A. M.; Liu, Y.; Mo, Y. Solid-State Chemistries Stable with High-Energy Cathodes for Lithium-Ion Batteries. *ACS Energy Lett.* **2019**, *4* (10), 2444−2451.
(75) Colón, J. L.; Thakur, D. S.; Yang, C.-Y.; Clearfield, A.; Martini, C. R. X-ray photoelectron spectroscopy and catalytic activity of α-zirconium phosphate and zirconium phosphate sulfophenylphosphonate. *J. Catal.* **1990**, *124* (1), 148−159.
(76) Wang, L.; Chen, B.; Ma, J.; Cui, G.; Chen, L. Reviving lithium cobalt oxide-based lithium secondary batteries-toward a higher energy density. *Chem. Soc. Rev.* **2018**, *47* (17), 6505−6602.
(77) Konar, R.; Maiti, S.; Shpigel, N.; Aurbach, D. Reviewing failure mechanisms and modification strategies in stabilizing high-voltage $LiCoO_2$ cathodes beyond 4.55V. *Energy Storage Mater.* **2023**, *63*, No. 103001.
(78) Zhang, S.; Zhao, F.; Wang, S.; Liang, J.; Wang, J.; Wang, C.; Zhang, H.; Adair, K.; Li, W.; Li, M.; Duan, H.; Zhao, Y.; Yu, R.; Li, R.; Huang, H.; Zhang, L.; Zhao, S.; Lu, S.; Sham, T.-K.; Mo, Y.; Sun, X. Advanced High-Voltage All-Solid-State Li-Ion Batteries Enabled by a Dual-Halogen Solid Electrolyte. *Adv. Energy Mater.* **2021**, *11* (32), No. 2100836.
(79) Prescher, C.; Prakapenka, V. B. DIOPTAS: a program for reduction of two-dimensional X-ray diffraction data and data exploration. *High Press. Res.* **2015**, *35* (3), 223−230.
(80) Yang, X.; Juhas, P.; Farrow, C. L.; Billinge, S. J. L. *xPDFsuite: an end-to-end software solution for high throughput pair distribution function transformation, visualization and analysis*, 2014, Preprint at http://arxiv.org/abs/1402.3163.
(81) Kresse, G.; Furthmüller, J. Efficient iterative schemes for ab initio total-energy calculations using a plane-wave basis set. *Phys. Rev. B* **1996**, *54* (16), 11169−11186.
(82) Perdew, J. P.; Burke, K.; Ernzerhof, M. Generalized Gradient Approximation Made Simple. *Phys. Rev. Lett.* **1996**, *77* (18), 3865−3868.
(83) Jain, A.; Ong, S. P.; Hautier, G.; Chen, W.; Richards, W. D.; Dacek, S.; Cholia, S.; Gunter, D.; Skinner, D.; Ceder, G.; Persson, K. A. Commentary: The Materials Project: A materials genome approach to accelerating materials innovation. *APL Mater.* **2013**, *1* (1), No. 011002.

https://doi.org/10.1021/acsami.4c08915
ACS Appl. Mater. Interfaces 2024, 16, 49328−49336